

Scalable Multi-Layer Printing of Graphene Interfacial Layers for Ultra-High Power Lithium-Ion Storage

Sang Ho Lee, Colin Johnston and Patrick S. Grant*

Dr. S. H. Lee, Dr. C. Johnston and Prof. P. S. Grant
Department of Materials, University of Oxford, Oxford OX1 3PH, UK
E-mail: sangho.lee@materials.ox.ac.uk

Keywords: graphene interfacial layer, $\text{Li}_4\text{Ti}_5\text{O}_{12}$, multi-layer, spray printing, lithium-ion capacitor

A low resistance graphene-based interfacial layer is developed for multi-layered lithium-ion capacitor electrodes using a layer-by-layer printing approach, with the goal of boosting energy storage performance at ultra-fast charge/discharge rates (≥ 100 C). The electrochemical behavior of spray printed $\text{Li}_4\text{Ti}_5\text{O}_{12}$ -based hetero-structure electrodes is investigated as a thin, discrete graphene layer is placed: (i) at the base of the $\text{Li}_4\text{Ti}_5\text{O}_{12}$ (at the electrode/current collector interface); (ii) on the top of the $\text{Li}_4\text{Ti}_5\text{O}_{12}$ (at the electrode/separator junction); and (iii) both at the base and on the top of the $\text{Li}_4\text{Ti}_5\text{O}_{12}$ (sandwich configuration), with marked improved electrode performance at > 50 C when the graphene layer is interleaved at the $\text{Li}_4\text{Ti}_5\text{O}_{12}$ /current collector interface. This best performing hetero-structure negative electrode is then coupled with a spray printed activated carbon positive electrode in a lithium-ion capacitor configuration, showing an attractive power density of ~ 8000 W/kg at 350 C. The fabrication of double-sided graphene/ $\text{Li}_4\text{Ti}_5\text{O}_{12}$ multi-layered hetero-electrodes is successfully demonstrated over areas of $20\text{ cm} \times 15\text{ cm}$ and in various patterned configurations.

1. Introduction

The lithium-ion battery (LIB) is the predominant energy storage technology for mobile and electric vehicle applications because of its relatively high energy density (~ 300 Wh/kg and ~ 700 Wh/L), useful cell voltage (~ 4 V) and low self-discharge that are available at a steadily reducing cost due to expanding global production capacity.^[1-4] However, LIBs have relatively low power density (300-400 W/kg) that in practice means charge times are unhelpfully long, performance is relatively poor at fast discharge (≥ 5 C), and capacity fades relatively quickly as charge/discharge cycles are repeated (< 500 cycle life). To provide an alternative balance of capacity, power density and cycle life, hybrid lithium-ion capacitors (LIC) have been developed that comprise an insertion-type negative electrode (similar to a LIB) and an activated carbon (AC)-based positive electrode (similar to an electrochemical capacitor) in a standard LIB electrolyte, which have shown power as high as 2-10 kW/kg over thousands of charge/discharge cycles.^[5-8]

Spinel-type $\text{Li}_4\text{Ti}_5\text{O}_{12}$ (LTO) is a promising negative electrode material for LIC applications because it has approximately zero-strain on lithium-ion insertion that can provide useful capacity even at > 10 C, a relatively high lithiation potential (~ 1.55 V (vs. Li/Li^+)) and a low rate of capacity degradation over 500 charge/discharge cycles. LTO is superior in terms of capacity and cycle stability over commonly used graphite under high rate conditions.^[9-13] LTO can also be used without the need for a pre-lithiation process that helps to reduce processing costs. However, when compared with the electrochemical double layer capacitive mechanism of the AC positive electrode in a LIC configuration, the LTO has comparatively sluggish insertion kinetics, and its relatively poor electronic conductivity ($\sim 10^{-3}$ S/cm) eventually restricts the overall LIC power performance. The dynamic response of LICs may be improved by contriving the negative electrode microstructure to have a higher porosity fraction and lower pore tortuosity, and by modifying the resistance of the electrode arrangement. In the case of the interface at the electrode/current collector, carbonaceous

interfacial layers have been interleaved between electrodes and current collector to improve charge transport kinetics and possibly even to facilitate the relaxation of electrode stress in LIB applications.^[14-16] Patterned microstructures or adhesive layers have also been integrated into the membrane electrode assemblies of fuel cells, leading to marked improvements in ion mobility and reduced contact resistance between electrodes and electrolyte.^[17-19] Various metal oxides or graphene oxide-based interface layers have also been useful to improve optical absorption, hole transport, or shunt and series resistance in both organic and inorganic solar cells.^[20-22]

In this paper, graphene (G) layers are investigated to reduce the interfacial resistance of LTO negative electrodes in LICs and are shown to facilitate excellent LIC performance at ultra-fast charging rates of ≥ 100 C. We assemble hetero-layered structures directly onto large area current collectors by spray printing of thin G layers and LTO electrodes, layer-by-layer, in a single operation. Initially, the location of G layers is studied: (i) at the LTO/current collector interface; (ii) at the LTO/separator interface; and (iii) at both interfaces (sandwich configuration). The highest performing LTO-based negative electrode in a half-cell is then paired with a spray printed commercial activated carbon (YP-50F, YP) positive electrode, providing a stable energy density of ~ 50 Wh/kg at 0.1 C and an attractive power density of ~ 8000 W/kg at 350 C (at ~ 23 Wh/kg) in a full LIC arrangement, which outperformed a spray printed LIC using a LTO-only electrode (~ 7000 W/kg at the same rate). The G-LTO hetero-layered structure was also developed into a double-sided configuration over $20\text{ cm} \times 15\text{ cm}$ current collectors to show scalability, along with the ability to selectively pattern areas of the printed electrode.

2. Results and discussion

Figure 1 shows schematically the fabrication of multi-layers of G and LTO, layer-by-layer, using the scalable spray printing process. A stable, relatively dilute feedstock suspension ($< \sim 5 \times 10^{-3}$ g/mL) is required to ensure consistent pumping and flow of the suspension to the spray nozzle and the stable atomization of the suspension into droplets that are projected onto the heated current collector foil substrate (the detailed suspension preparation is described in the experimental section). The current collector is continuously heated throughout deposition on a vacuum chuck (> 120 °C) so there is almost immediate drying of deposited suspension droplets. The successive superimposition of layers of deposited droplets over the pre-formed structure assembles the final electrode. The arrangement of G and LTO layers in the multi-layered structure is tailored simply by switching between G or LTO containing feedstock suspensions during deposition. This freedom in design for discrete layers and various types of grading^[23-29] is not available by conventional slurry casting manufacture of LIB and LIC electrodes, and was investigated to obtain more attractive balance of overall LIC performance. Layer thicknesses, from a few microns to the millimeter scale, can be controlled simply by the number of times the spray scan is repeated. The use of multiple nozzles could be helpful to increase throughput towards small scale commercial manufacture and/or a semi-continuous roll-to-roll implementation.

Figures 2a-c show a series of electrode cross-section scanning electron microscope (SEM) images prepared using precision etching and coating system (PECS) milling. The effect of the position of the discrete G layer was investigated: (a) at the base of LTO, next to the current collector (denoted as G-LTO hereafter), (b) both at the base and on the top of LTO, a sandwich configuration (G-LTO-G), and (c) on the top of LTO, closest to the separator/cathode (LTO-G). The inset images in the corner of each figure magnify the G interfacial layer in the hetero-structure. It was noted that a few micron-scale pores were formed spontaneously in the discrete G layer when it was deposited directly onto the heated

current collector, as shown in the left corner insets of Figure 2a (the G-LTO) and Figure 2b (the G-LTO-G). As shown in previous studies, these pore structures can be useful in facilitating the dispersion of electrochemically active lithium-ions throughout the electrode, and can promote capacity at fast charging rates (≥ 20 C).^[30-34] The thickness of the G layer interleaved between the LTO and current collector was ~ 1 μm , and the G layer on the top of LTO was ~ 2 μm . Overall, all the multi-layered hetero-electrodes were ~ 20 μm thick (see Table 1). Here, this relatively thin electrode was chosen because high power performance in particular was sought, and a thicker intercalation negative electrode would require an ever thicker electrochemical double layer positive electrode to stay in charge balance in a full cell, at which point restricted lithium-ion availability in some parts of the electrode starts to inhibit electrode dynamics.

Figure 3a shows the comparative discharge capacity performance of the four electrode configurations as a function of C-rate. In the range of 0.1 to 10 C, the G layer made little difference to the discharge capacity (see the magnified inset of Figure 3a) because there was sufficient time in each cycle for lithium-ions (and electrons) to disperse throughout the electrode, so almost all the available active materials/sites were utilized. However, as the C-rate increased to 50 C, the difference in capacity became more marked as a function of the G position. At 50 C, the G-LTO multi-layered electrode had the highest capacity (~ 80 mAh/g), representing an approximately 60 % improvement in deliverable discharge capacity when compared with the LTO-only electrode (~ 50 mAh/g). Note that the capacity was estimated based on the total electrode mass including LTO, Super P conductive carbon (SP), polymeric binder (carboxymethyl cellulose, CMC) and G (refer to Table 1). At 50 C, the G-LTO-G electrode had capacity similar to the G-LTO, whereas the LTO-G arrangement showed no meaningful capacity benefit when compared with LTO-only. Overall, the G interfacial layer was helpful only at ultra-fast rates of > 50 C and when the G layer was interleaved between the electrode and current collector.

The effect of the G interfacial layer was further investigated using electrochemical impedance spectroscopy (EIS). In the Nyquist plots of Figure 3b, the semi-circles in the high/medium frequency region indicated the charge transport resistance within the overall electrode, while the inclined lines in the low frequency range corresponded to the Warburg impedance that related to the ion diffusion within the electrode.^[35,36] Consistent with the trend in the rate performance (Figure 3a), the G-LTO electrode showed a reduction in electrode charge transport resistance particularly when compared with the LTO-only and LTO-G electrode. Figure 3c shows the galvanostatic discharge plots at 10 C for the same electrodes. After 500 cycles, the G-LTO electrodes sustained the highest discharge capacity of 128 mAh/g, while the G-LTO-G, LTO-G and LTO-only electrodes had slightly lower discharge capacities of 125 mAh/g, 123 mAh/g and 120 mAh/g, respectively. This data indicated that the thin, discrete G layer interleaved between the LTO electrode and the current collector reduced the resistance at the interface of electrode/current collector and improved long-term cycling performance. All electrodes sustained a coulombic efficiency of almost 100 % up to the 500th cycle, as shown in the inset of Figure 3c.

To clarify any intrinsic benefit of a discrete G layer, an electrode comprising randomly mixed LTO and G with the same weight fraction of 98 wt% LTO and 2 wt% G was prepared using identical spray printing parameters, noting that the weight fraction of LTO and G was calculated based on the loading mass of the G-LTO electrode, as given in Table 1. This provided for a fair comparison with the best performing G-LTO multi-layered hetero-structure. Figure S1 in Supporting Information shows electrode cross-sections of the random mixture of G and LTO (denoted as RM), with G flakes distributed apparently randomly. The RM electrode thickness was again ~ 20 μm (see Table S1 in the Supporting Information).

Figure S2a shows comparative capacity versus C-rate performance data for the G-LTO, LTO-only and RM electrodes, noting that the capacity was again estimated using the total electrode weight of LTO, G, SP and CMC. As before, in the range of 0.1 to 10 C the

electrodes had similar capacities regardless of G addition, while at 50 C the G-LTO electrode (~ 80 mAh/g) had a slightly higher capacity than the RM equivalent (~ 70 mAh/g), which had higher capacity than LTO-only (~ 50 mAh/g). The corresponding Nyquist plots in Figure S2b of the Supporting Information showed a slightly improved interfacial resistance of G-LTO ($\sim 105 \Omega$) over RM ($\sim 115 \Omega$), both of which were superior to LTO-only ($\sim 135 \Omega$). Overall, adding extra 2 wt% of G flakes in electrodes reduced electrode resistance and increased charge/discharge capacity at ultra-fast rates, especially when the G flakes were used as a discrete, interfacial layer between the electrode and the current collector.

The influence of the G interfacial layer was then investigated in a full LIC configuration, where the best performing G-LTO negative electrode was paired with a spray printed YP positive electrode, as shown schematically in the inset of Figure 4a (the half-cell performance of spray printed YP electrodes are shown in Figure S3 of the Supporting Information). Figure 4a shows comparative Ragone plots for LICs using the G-LTO and LTO-only electrodes, where the total electrode mass ratio of LTO:YP was 1:5. Power P and energy E were estimated using $P [\text{W}] = V \times i / m$ and $E [\text{Wh}] = P \times t$, where V was the average cell potential [V] between the lowest and highest cut-off potential, i was the delivered current [A], m was the total mass of both anode and cathode electrodes including LTO, G, YP, SP and CMC (see Table 2), and t was the discharge time [h].^[37,38] Similarly to the half-cell performance, the G interfacial layer made little difference in overall LIC performance at 0.1 C, with an energy density of ~ 50 Wh/kg for both the electrodes. However, at 350 C the G-LTO electrode delivered a markedly improved power density of ~ 8000 W/kg (at ~ 23 Wh/kg) compared with the LTO-only electrode (~ 7000 W/kg).

Figure 4b shows the gravimetric charge/discharge curves for LIC using the G-LTO and LTO-only electrodes. Capacitance C was estimated using $C [\text{F/g}] = i \times t / V$, where i was the applied current [A/g], t was the discharge or charge time [s], and V was the potential difference [V].^[32,39] At a current density of 3.5 A/g, the G-LTO electrode (~ 46 F/g) provided

~ 40 % improvement in a deliverable capacitance when compared with the LTO-only electrode (~ 33 F/g).

Figure 4c shows the galvanostatic discharge energy density at 10 C for LIC cells based on the G-LTO and LTO-only electrodes. After 2000 cycles, the G-LTO and LTO-only electrodes delivered energy densities of ~ 35 Wh/kg and ~ 25 Wh/kg, respectively, representing ~ 75 % and ~ 50 % of the initial energy density (~ 47 Wh/kg of the 1st cycle for both electrodes), respectively, as shown in the right-hand inset of Figure 4c. The left-hand inset of Figure 4c shows the double-sided fabrication of a spray printed electrode on an A5-area Cu current collector (~ 20 cm × 15 cm), showing practical scalability to the manufacture of pouch cell-based packs, for example for automotive applications. Furthermore, the G-LTO hetero-structure could be also fabricated selectively in patterned areas (the inset of Figure 4c), supporting the extra flexibility of the multi-layer printing approach to large-area electrode manufacturing. For example, the ion and electron mobility within pouch cells is known to vary according to the distance from the pouch cell tabs^{24,35} so that the corners furthest from the tabs have provide very poor fractions of active material utilization, especially at ultra-fast charging rates. Using a patterning strategy, more conductive layers (e.g. G layers as used here) or higher capacity components (Si, SnO₂ or Ge) can be selectively added into the electrodes by spray printing in order to tailor local electrode properties and to boost overall cell performance.

The preceding results show that the thin G layer reduced interfacial resistance at the electrode/current collector, improving overall electrode charge transport, as described in the cartoon in Figure 5a. However, there was also an additional effect that G layers also induced an increase in the local electrode porosity at the junction between LTO and G, as shown in the electrode cross-section SEM image in Figure 5b. Consistent with previous work,^[30-32] this local porosity will facilitate ion mobility in the region of the electrode/current collector

junction particularly at ultra-fast charge/discharge rates (≥ 400 C), where otherwise lithium-ion “starvation” may occur,^[40-42] as depicted in the idealized graphical illustration in Figure 5a.

The G-LTO multi-layer-based LIC was compared with other LTO/AC-based LIC cells from the literature, as shown in Figure 5c.^[43-47] At relatively slow charging rates, the energy density was comparable with other LIC arrangements. However, at ultra-fast charging rates (≥ 400 C) the G-LTO LIC was at least similar or superior to similar configurations (also see detailed comparison in Table S3 of the Supporting Information). It should be recognized that many of apparently similar data relied on much higher fractions of parasitic inactive components (≥ 20 wt%) than used here (5 wt%), the mass of which were not taken into account in the gravimetric/volumetric performance estimation.

3. Conclusion

The influence of the interfacial layer comprising graphene with well-known high electrical conductivity on the electrochemical performance of lithium-ion capacitors has been investigated. In order to form these hetero-electrodes, a layer-by-layer spray printing approach was used that allowed the position of G layers to be placed anywhere within the plane of the electrode. When thin G layers were interleaved between the LTO and current collector, the resulting interfacial layer played a crucial role in reducing resistance and increasing local porosity to boost LIC rate capability at ultra-fast charging rates, with an attractive power density of ~ 8000 W/kg at 350 C and ~ 75 % of initial energy density after 2000 cycles. Layer-by-layer structuring of different but complementary materials combinations in scalable multi-layered configurations is shown to deliver performance benefits or performance combinations that are unavailable by conventional electrode manufacturing routes. More broadly, the approach allows increased freedom to realize a greater range of thickness, composition and geometrical arrangement of materials for better functionality and more efficient materials utilization.

4. Experimental Section

Materials: LTO and CMC were obtained from Sigma Aldrich, UK; G from Graphene Laboratories INC, USA; SP from MTI, USA; and YP from Kuraray, Japan.

Spray printing process: For the spray suspension, LTO (or YP), SP and CMC in a controlled mass ratio of 95:3:2 were suspended into a mixture of deionized (DI) water and isopropyl alcohol (IPA) at a DI:IPA volume ratio of 60:40 that had optimum stability without any sediment or suspended particles, and provided the best deposition efficiency of electrode constituents onto the current collector, as reported in previous work.^[31] While DI water was required to dissolve CMC, IPA helped to disperse carbon materials. In the case of the G suspension, G and CMC were formulated in a 95:5 mass ratio in the same fugitive solvent mixture. Prior to the spray process, a current collector (e.g. stainless steel discs, Cu or Al foils) was fixed on a vacuum chuck and hot plate that was set to a temperature higher than the boiling point of both the IPA and DI water, for example at > 120 °C. The suspension was then pumped to a spray nozzle and subsequently atomized at a constant compressed air pressure of 0.4 bar while the spray nozzle moved in a pre-programmed zig-zag pattern in the x and y plane above the substrate at a fixed spray distance z . All spray processes were carried out in a well-ventilated fume cupboard. For patterned electrode structures, rectangular or circular metal shadow masks were placed on a region of the current collector before the spray printing process. The electrode layers were then printed through the masks.

Electrochemical tests: The electrochemical performance of spray printed electrodes was investigated using coin-type electrochemical cells (CR2032) that were assembled from thoroughly dried electrodes in an Ar-filled glovebox ($\text{H}_2\text{O} < 0.1$ ppm, $\text{O}_2 < 0.1$ ppm). For half-cell tests, LTO-based electrodes were coupled with high purity lithium foils (99.9% trace metals basis, MTI, USA) that were used as a counter/reference electrode. In the case of full LIC cells, spray printed anodes (e.g. LTO-only or G-LTO multi-layered electrodes) were

coupled with spray printed YP cathodes. All the LICs were formulated with a 1:5 anode:cathode capacity ratio, as given in Table 2. The anodes and cathodes were electrically separated by a polypropylene separator (Celgard 2400, UK) soaked in 1 M LiPF₆ electrolyte solution in a 1:1 mixture (by volume) of ethylene carbonate and dimethyl carbonate (Sigma-Aldrich, UK). Charge/discharge cycling for both half-cells and full LICs was carried out at room temperature using Arbin BT2000 cyclers. The capacities of half-cells were obtained on the basis of the total electrode mass including LTO, G, SP and CMC. Full LIC performance was estimated using the total mass of anode and cathode electrodes (Table 2). CV and EIS measurements were carried out using Gamry 600 potentiostats. The theoretical capacity of LTO was assumed to be ~ 175 mAh/g.^[9,10]

Supporting Information

Supporting Information is available from the Wiley Online Library or from the author.

Acknowledgements

This work was supported by Innovate UK grant number 102655 “ALICE – Advanced Lithium Ion Capacitors and Electrodes”.

Received: ((will be filled in by the editorial staff))

Revised: ((will be filled in by the editorial staff))

Published online: ((will be filled in by the editorial staff))

References

- [1] X. Zhou, L. Yu, X. –Y. Yu, X. W. Lou, *Adv. Energy Mater.* **2016**, 6, 1601177.
- [2] S. H. Lee, W. B. Kim, *J. Power Sources* **2016**, 307, 38.
- [3] M. Winter, B. Barnett, K. Xu, *Chem. Rev.* **2018**, 118, 11433.
- [4] M. Li, J. Lu, Z. Chen, K. Amine, *Adv. Mater.* **2018**, 30, 1800561.
- [5] A. Jagadale, X. Zhou, R. Xiong, D. P. Dubal, J. Xu, S. Yang, *Energy Storage Mater.* **2019**, 19, 314.
- [6] J. Ding, W. Hu, E. Paek, D. Mitlin, *Chem. Rev.* **2018**, 118, 6457.

- [7] Q. Lu, B. Lu, M. Chen, X. Wang, T. Xing, M. Liu, X. Wang, *J. Power Sources* **2018**, 398, 128.
- [8] E. Zhao, C. Qin, H. –R. Jung, G. Berdichevsky, A. Nese, S. Marder, G. Yushin, *ACS Nano* **2016**, 10, 3977.
- [9] C. Han, Y. –B. He, M. Liu, B. Li, Q. –H. Yang, C. –P. Wong, F. Kang, *J. Mater. Chem. A* **2017**, 5, 6368.
- [10] L. Wu, X. Leng, Y. Liu, S. Wei, C. Li, G. Wang, J. Lian, Q. Jiang, A. Nie, T. –Y. Zhang, *ACS Appl. Mater. Interfaces* **2017**, 9, 4649.
- [11] X. Sun, P. V. Radovanovic, B. Cui, *New J. Chem.* **2015**, 39, 38.
- [12] T. Liang, X. Liu, X. Liu, X. Guan, C. Wang, A. Fu, Y. Li, P. Guo, H. Li, *Energy Technol.* **2018**, 6, 2036.
- [13] C. Y. Bon, P. Isheunesu, S. Kim, M. Manasi, Y. I. Kim, Y. J. Lee, J. M. Ko, *Energy Technol.* **2018**, 6, 2461.
- [14] S. H. Lee, Y. Noh, Y. –R. Jo, Y. Kim, B. –J. Kim, W. B. Kim, *Energy Technol.* **2018**, 6, 1255.
- [15] C. Huang, J. Zhang, H. J. Snaith, P. S. Grant, *ACS Appl. Mater. Interfaces* **2016**, 8, 20756.
- [16] F. Xia, S. Kwon, W. W. Lee, Z. Liu, S. Kim, T. Song, K. J. Choi, U. Paik, W. I. Park, *Nano Lett.* **2015**, 15, 6658.
- [17] S. H. Lee, W. Park, B. H. Lee, W. B. Kim, *J. Mater. Chem. A* **2015**, 3, 13492.
- [18] Z. Yang, T. Fujigaya, N. Nakashima, *J. Power Sources* **2015**, 300, 175.
- [19] C. –C. Sung, C. –Y. Liu, C. C. J. Cheng, *Int. J. Hydrog. Energy* **2014**, 39, 11700.
- [20] A. Bashir, J. H. Lew, S. Shukla, D. Gupta, T. Baikie, S. Chakraborty, R. Patidar, A. Bruno, S. Mhaisalkar, Z. Akhter, *Sol. Energy* **2019**, 182, 225.
- [21] B. Zhao, G. Niu, Q. Dong, J. Liu, N. Li, J. Li, L. Wang, *J. Mater. Chem. A* **2018**, 6, 23797.

- [22] L. Zhou, D. Yang, W. Yu, J. Zhang, C. Li, *Org. Electron.* **2015**, 23, 110.
- [23] S. H. Lee, C. Huang, P. S. Grant, *Nano Energy* **2019**, 61, 96.
- [24] C. Huang, N. P. Young, J. Zhang, H. J. Snaith, P. S. Grant, *Nano Energy* **2017**, 31, 377.
- [25] C. Cheng, R. Drummond, S. R. Duncan, P. S. Grant, *J. Power Sources* **2020**, 448, 227376.
- [26] C. Cheng, R. Drummond, S. R. Duncan, P. S. Grant, *J. Power Sources* **2019**, 413, 59 59.
- [27] K. -H. Choi, D. B. Ahn, S. -Y. Lee, *ACS Energy Lett.* **2018**, 3, 220.
- [28] Y. Wu, H. Wu, S. Luo, K. Wang, F. Zhao, Y. Wei, P. Liu, K. Jiang, J. Wang, S. Fan, *RSC Adv.* **2014**, 4, 20010.
- [29] N. Singh, C. Galande, A. Miranda, A. Mathkar, W. Gao, A. L. M. Reddy, A. Vlad, P. M. Ajayan, *Sci. Rep.* **2012**, 2, 481.
- [30] S. H. Lee, A. Mahadevegowda, C. Huang, J. D. Evans, P. S. Grant, *J. Mater. Chem. A* **2018**, 6, 13133.
- [31] S. H. Lee, K. Li, C. Huang, J. D. Evans, P. S. Grant, *ACS Appl. Mater. Interfaces* **2019**, 11, 603.
- [32] S. H. Lee, C. Johnston, P. S. Grant, *ACS Appl. Mater. Interfaces* **2019**, 11, 37859.
- [33] J. Bu, P. Leung, C. Huang, S. H. Lee, P. S. Grant, *J. Mater. Chem. A* **2019**, 7, 19094.
- [34] C. Huang, P. S. Grant, *J. Mater. Chem. A* **2018**, 6, 14689.
- [35] S. H. Lee, C. Huang, C. Johnston, P. S. Grant, *Electrochim. Acta* **2018**, 292, 546.
- [36] S. H. Lee, Y. -R. Jo, Y. Noh, B. -J. Kim, W. B. Kim, *J. Power Sources* **2017**, 367, 1.
- [37] C. Huang, J. Zhang, N. P. Young, H. J. Snaith, P. S. Grant, *Sci. Rep.* **2016**, 6, 25684.
- [38] C. Fu, A. Mahadevegowda, P. S. Grant, *J. Mater. Chem. A* **2016**, 4, 2597.
- [39] Y. Sun, J. Tang, F. Qin, J. Yuan, K. Zhang, J. Li, D. -M. Zhu, L. -C. Qin, *J. Mater. Chem. A* **2017**, 5, 13601.
- [40] E. Hosseinzadeh, R. Genieser, D. Worwood, A. Barai, J. Marco, P. A Jennings, *J. Power Sources* **2018**, 382, 77.

- [41] S. J. Bazinski, X. Wang, *J. Electrochem. Soc.* **2014**, *161*, A2168.
- [42] L. Cai, K. Ana, Z. Feng, C. Liang, S. J. Harris, *J. Power Sources* **2013**, *236*, 163.
- [43] B. Li, H. Zhang, D. Wang, H. Lv, C. Zhang, *RSC Adv.* **2017**, *7*, 37923.
- [44] H. Kim, K. -Y. Park, M. -Y. Cho, M. -H. Kim, J. Hong, S. -K. Jung, K. C. Roh, K. Kang, *ChemElectroChem* **2014**, *1*, 125.
- [45] H. Xu, X. Hu, Y. Sun, W. Luo, C. Chen, Y. Liu, Y. Huang, *Nano Energy* **2014**, *10*, 163.
- [46] Y. Lei, Z. -H. Huang, Y. Yang, W. Shen, Y. Zheng, H. Sun, F. Kang, *Sci. Rep.* **2013**, *3*, 2477.
- [47] V. Aravindan, D. Mhamane, W. C. Ling, S. Ogale, S. Madhavi, *ChemSusChem* **2013**, *6*, 2240.

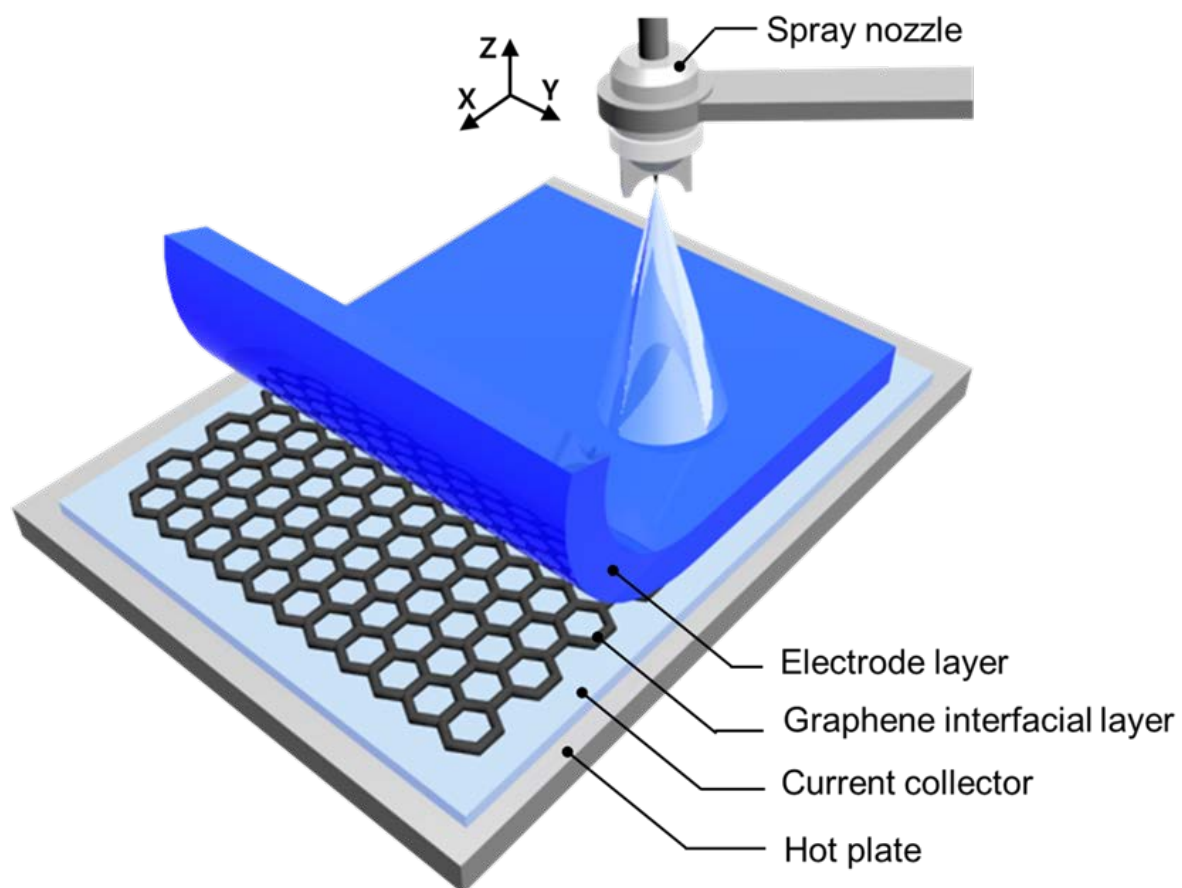


Figure 1. Graphical illustration of the layer-by-layer spray printing of the G interfacial layer and the LTO electrode into multi-layered hetero-electrodes.

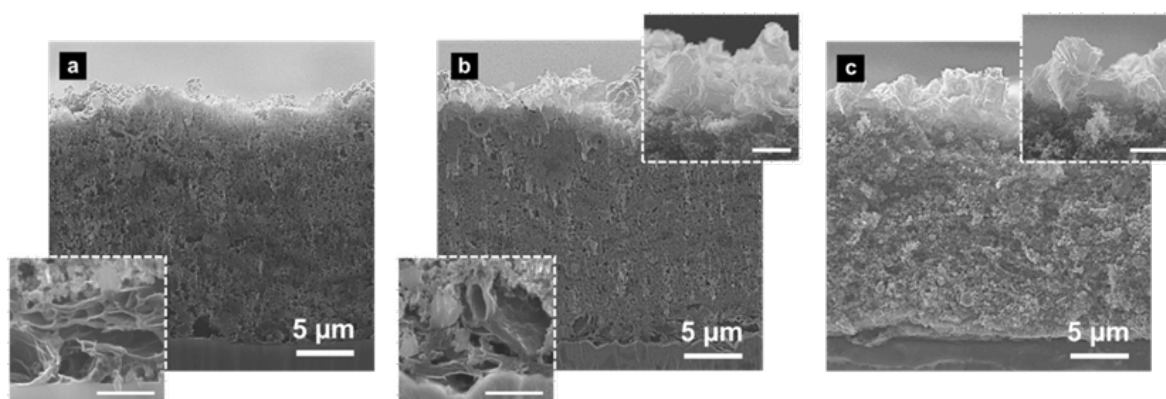


Figure 2. Cross-section SEM images of multi-layered hetero-structures as a function of the G layer location: (a) at the base of the LTO layer (G-LTO), (b) both at the base and on the top of the LTO (G-LTO-G) and (c) on the top of the LTO (LTO-G). Each inset magnifies the region of the interfacial G layer within the multi-layered structure. The inset scale bar indicates 1 μm .

Table 1. Summary data for LTO-based electrodes as a function of the G location.

Electrode type	Loading mass (mg/cm ²)		Thickness (μm)	
	LTO	G	LTO	G
LTO-only	2.31 ± 0.04	0	20 ± 3	0
G-LTO	2.28 ± 0.04	0.04 ± 0.02	19 ± 3	1.0 ± 0.1
G-LTO-G	2.25 ± 0.04	0.09 ± 0.02	18 ± 3	2.9 ± 0.3
LTO-G	2.27 ± 0.03	0.04 ± 0.01	19 ± 2	2.0 ± 0.2

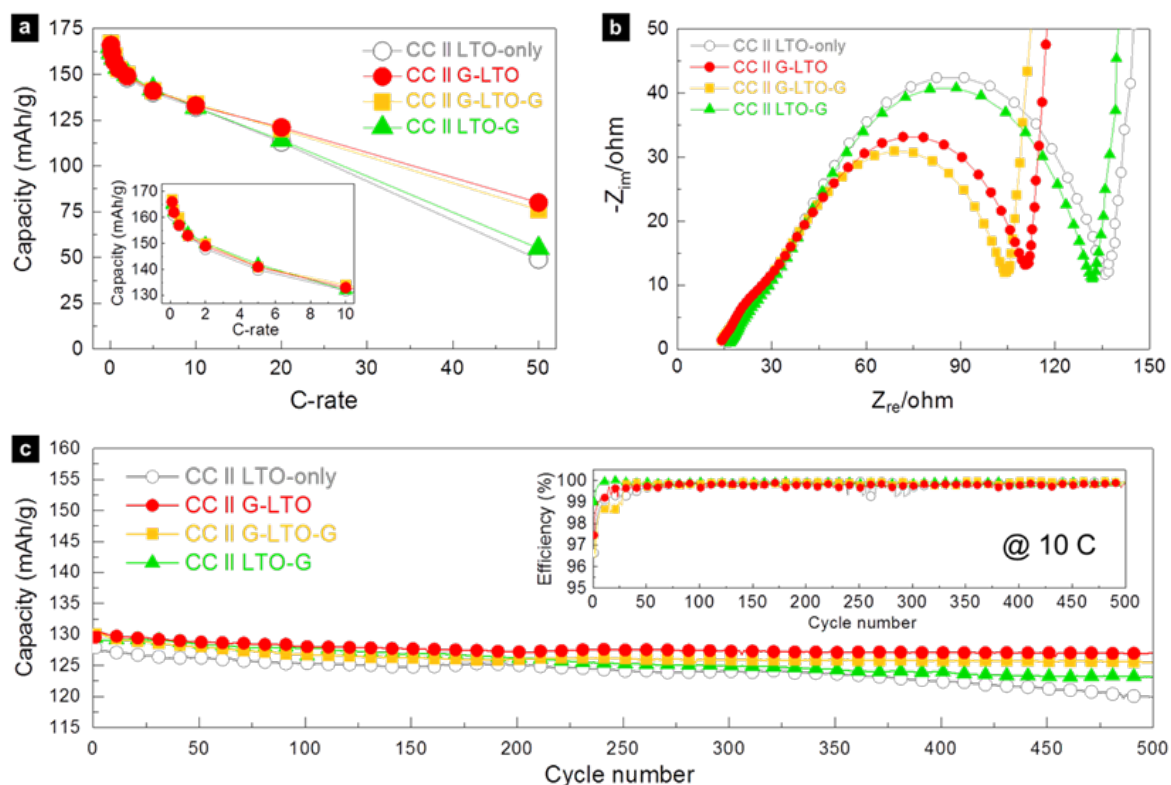


Figure 3. (a) Discharge capacity profiles of the spray printed LTO-based electrodes as a function of the position of discrete G layer arrangement in the potential range of 1.0 to 2.5 V (vs. Li/Li^+). The inset (the left corner) magnifies the range of 0.1 to 10 C. (b) Nyquist plots as a function of the G arrangement. (c) Galvanostatic discharge capacity profiles at 10 C in the voltage window of 1.0 to 2.5 V (vs. Li/Li^+) and the corresponding coulombic efficiency plots (inset).

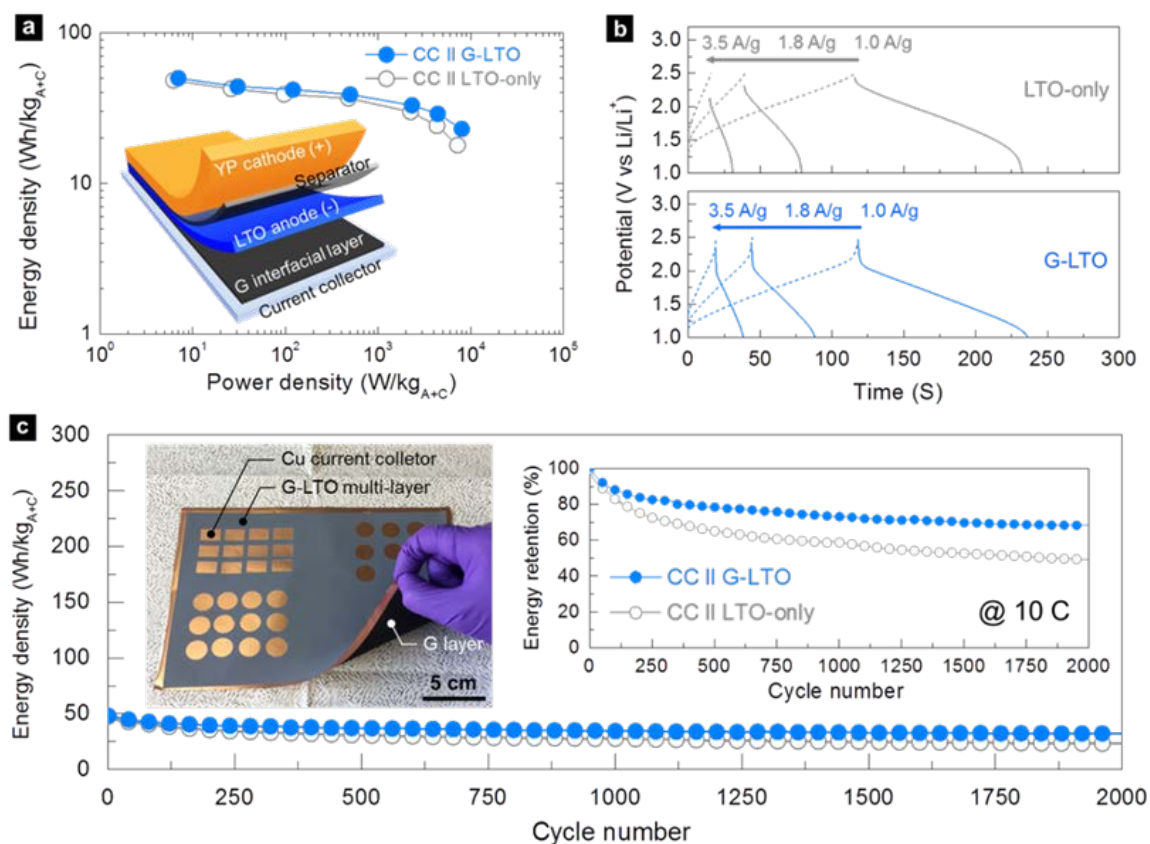


Figure 4. (a) Ragone plots for LICs using the G-LTO and LTO-only electrodes in the voltage range of 1.0 to 2.5 V (vs. Li/Li^+). The inset describes the arrangement of the G, LTO and YP layers in the LIC device. (b) Comparative charge/discharge curves at 1.0, 1.8 and 3.5 A/g in the voltage window 1.0 to 2.5 V (vs. Li/Li^+) for LICs using the G-LTO and LTO-only electrodes. (c) Galvanostatic discharge energy density plots at 10 C in the voltage range of 1.0 to 2.5 V (vs. Li/Li^+). The left-hand inset shows a photograph for double-sided fabrication over an A5 Cu current collector with the G-LTO hetero-structure formed on one side and a G interfacial layer only on the other side. The G-LTO electrode was patterned into rectangular and circular arrays. The right-hand inset shows the corresponding energy density retention as a function of cycle numbers.

Table 2. Summary data for the G-LTO and LTO-only electrodes in a LIC arrangement.

Anode type	Loading mass (mg/cm ²)		Thickness (μm)	
	Anode	YP cathode	Anode	YP cathode
LTO-only	2.32 ± 0.03	11.62 ± 0.07	20 ± 3	121 ± 3
G-LTO	2.34 ± 0.04	11.74 ± 0.05	21 ± 4	123 ± 5

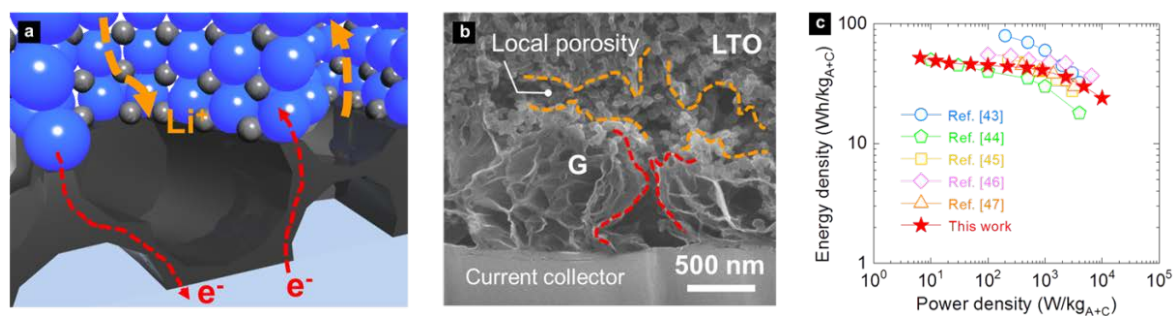


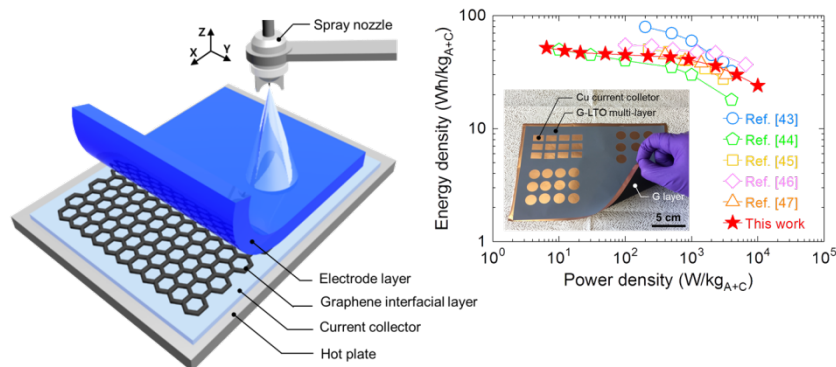
Figure 5. (a) Idealized schematic illustration of the ion and electron transport at the G/LTO interface. (b) An electrode cross-section SEM image of the interface between the G layer and the LTO electrode. The dotted lines indicate pore structures in the LTO (orange) and the G layer (red). (c) Comparative Ragone profiles.

The influence of a graphene interfacial layer on electrochemical performance of lithium-ion capacitors was investigated as a function of the position of the graphene layer within $\text{Li}_4\text{Ti}_5\text{O}_{12}$ -based high power hetero-electrodes.

Graphene interfacial layer, $\text{Li}_4\text{Ti}_5\text{O}_{12}$, multi-layer, spray printing, lithium-ion capacitor

S. H. Lee*, C. Johnston and P. S. Grant

Scalable Multi-Layer Printing of Graphene Interfacial Layers for Ultra-High Power Lithium-Ion Storage



Supporting Information

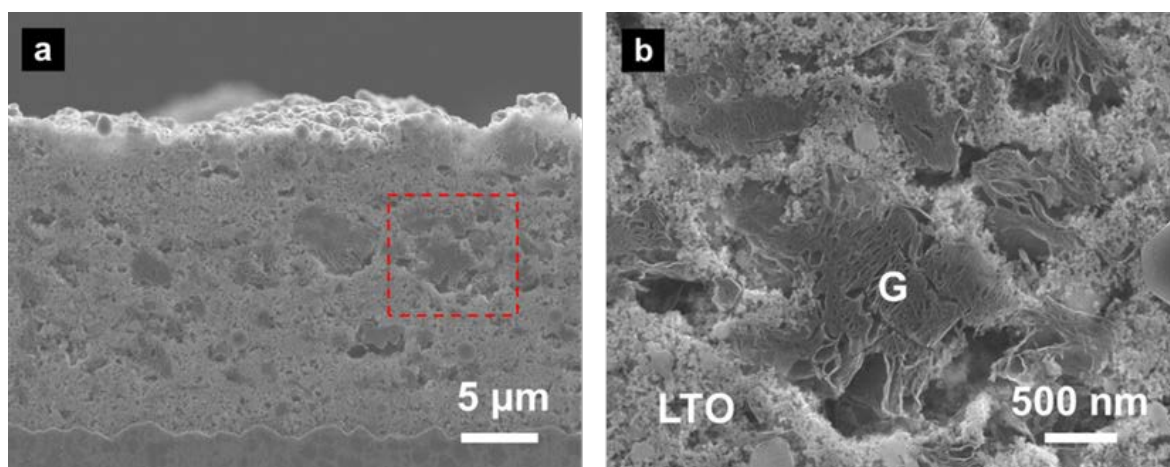
Scalable Multi-Layer Printing of Graphene Interfacial Layers for Ultra-High Power Lithium-Ion Storage*Sang Ho Lee*, Colin Johnston and Patrick S. Grant*

Figure S1. (a) Cross-section SEM image of the spray printed RM electrode. The red dotted box indicates the region of G flakes embedded within the LTO electrode. (b) Magnified image for the region including agglomerates of G flakes.

Table S1. Summary data for the spray printed LTO-based electrodes.

Electrode type	Mass loading (mg/cm ²)		Thickness (μm)	
	LTO	G	LTO	G
LTO-only	2.31 ± 0.04	0	20 ± 3	0
G-LTO	2.29 ± 0.04	0.05 ± 0.02	21 ± 3	1.0 ± 0.1
RM	2.31 ± 0.05		20 ± 3	

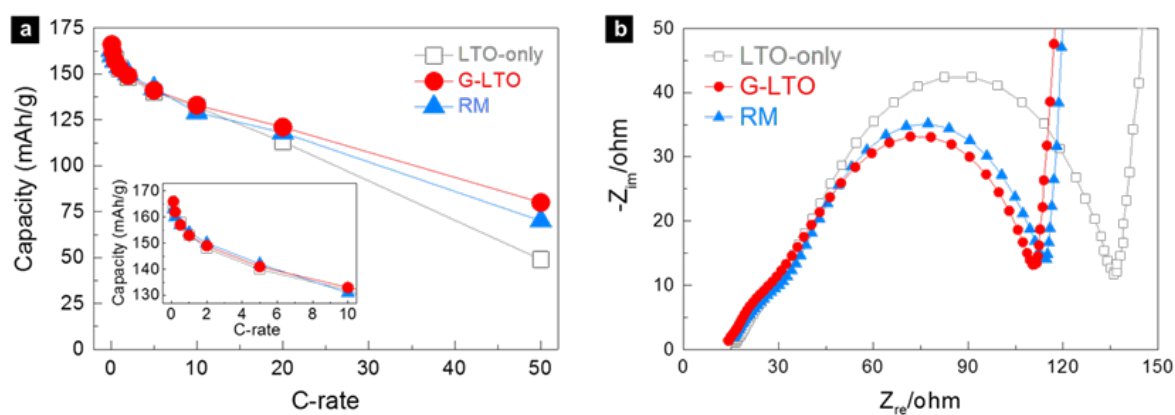


Figure S2. (a) Discharge capacity profiles for the G-LTO, LTO-only and RM electrodes at various rates in the potential range of 1.0 to 2.5 V (vs. Li/Li^+). The magnified inset shows the range of 0.1 to 10 C. (b) Nyquist curves for the G-LTO, LTO-only and RM electrodes.

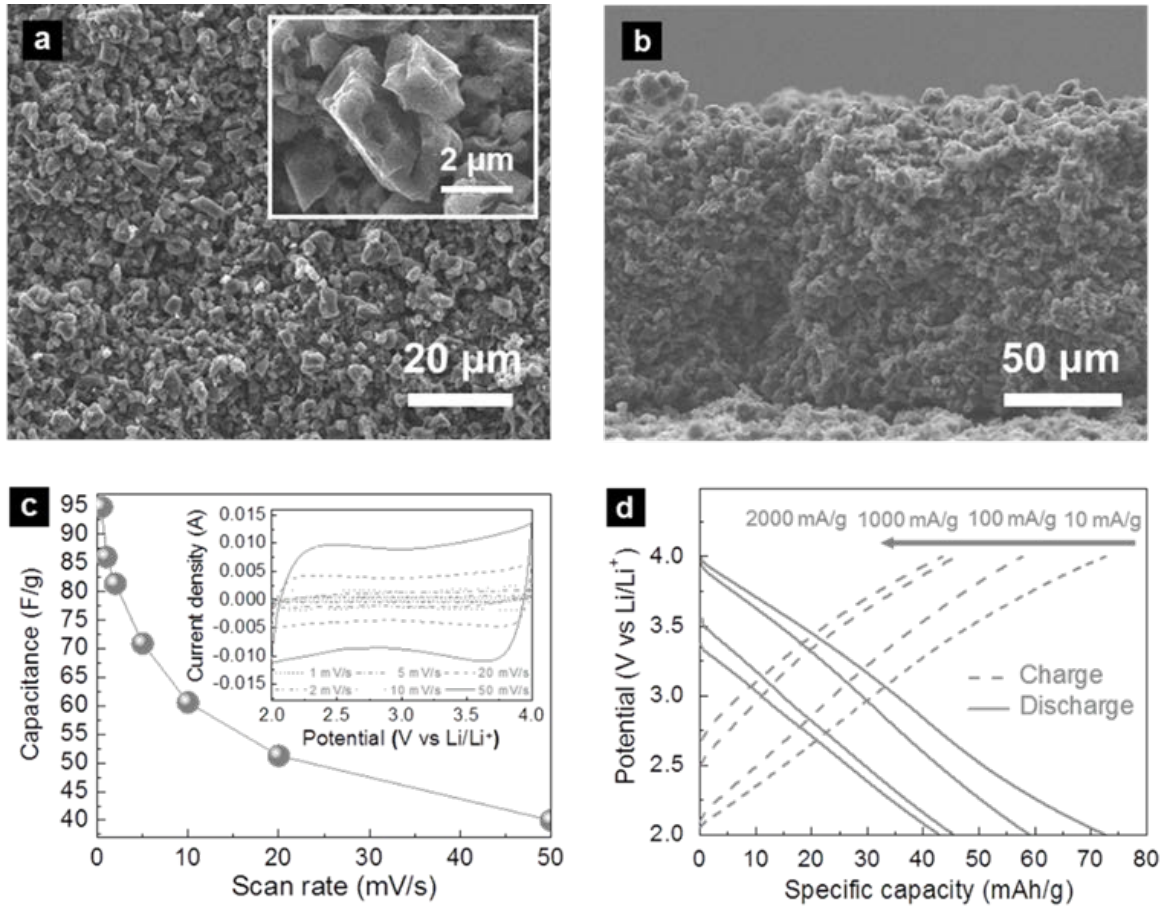


Figure S3. (a) SEM image of the surface of the spray printed YP electrode. The inset shows a magnified image of the region of YP particulates. (b) Cross-section image of the 120 μm thick YP electrode. (c) Specific capacitance profile for the spray printed YP electrode, which was estimated from the CV curves (the inset) according to:

$$C = \frac{1}{mv(V_a - V_c)} \int_{V_a}^{V_c} I(V) dV$$

where C was the specific capacitance [F/g], m was the total electrode mass [g], v was the scan rate [V/s], $V_a - V_c$ was the potential window [V], and I was the charging current [A]. The inset shows CV profiles at increasing scan rates (1 to 50 mV/s) in the potential range of 2.0 to 4.0 V (vs. Li/Li⁺). (d) Gravimetric charge/discharge capacity plots for the same YP electrode at 10, 100, 1000 and 2000 mA/g in the potential range of 2.0 to 4.0 V (vs. Li/Li⁺).

Table S2. Summary data for the spray printed YP electrode.

Formulation (YP : SP : CMC)	Mass loading (mg/cm ²)	Thickness (μm)	Discharge capacity (mAh/g)			
			10 mA/g	100 mA/g	1 A/g	2 A/g
95 : 3 : 2	11.73 ± 0.05	121 ± 5	72	58	46	43

Table S3. Comparative LIC performances.

Reference	Materials combination		Performances
	Anode (wt% ^[a])	Cathode (wt% ^[b])	
[43]	LTO (80)	AC (80)	Energy: 80 Wh/kg @ 2.5 C Power: 4000 W/kg @ 123 C
[44]	C-LTO (70)	Carbon nanofiber (70)	Energy: 50.3 Wh/kg @ 4.4 C Power: 3000 W/kg @ 109 C
[45]	Graphene-LTO (80)	AC (90)	Energy: 50 Wh/kg @ 0.4 C Power: 2500 W/kg @ 167 C
[46]	LTO (80)	Graphite (80)	Energy: 55 Wh/kg @ 1.8 C Power: 6500 W/kg @ 176 C
[47]	LTO (80)	Graphene (80)	Energy: 45 Wh/kg @ 6.7 C Power: 3300 W/kg @ 110 C
This work	Graphene-LTO (95)	YP-50F (95)	Energy: 53 Wh/kg @ 0.1 C Power: 8000 W/kg @ 350 C

^[a] Weight fraction of active materials within the anode electrode.

^[b] Weight fraction of active materials within the cathode electrode.